Direct measurement of protein–protein interactions by FLIM-FRET at UV laser-induced DNA damage sites in living cells

Tanja Kaufmann[1], Sébastien Herbert[1], Benjamin Hackl[1], Johanna Maria Besold[1], Christopher Schramek[1], Josef Gotzmann [2], Kareem Elsayad[3] and Dea Slade [1,*]

[1]Department of Biochemistry, Max Perutz Labs, University of Vienna, Vienna Biocenter (VBC), Dr Bohr-Gasse 9, 1030 Vienna, Austria, [2]Department of Medical Biochemistry, Max Perutz Labs, Medical University of Vienna, Vienna Biocenter (VBC), 1030 Vienna, Austria and [3]VBCF Advanced Microscopy Facility, Vienna Biocenter (VBC), Dr Bohr-Gasse 3, 1030 Vienna, Austria

ABSTRACT

Protein–protein interactions are essential to ensure timely and precise recruitment of chromatin remodellers and repair factors to DNA damage sites. Conventional analyses of protein–protein interactions at a population level may mask the complexity of interaction dynamics, highlighting the need for a method that enables quantification of DNA damage-dependent interactions at a single-cell level. To this end, we integrated a pulsed UV laser on a confocal fluorescence lifetime imaging (FLIM) microscope to induce localized DNA damage. To quantify protein–protein interactions in live cells, we measured Förster resonance energy transfer (FRET) between mEGFP- and mCherry-tagged proteins, based on the fluorescence lifetime reduction of the mEGFP donor protein. The UV-FLIM-FRET system offers a unique combination of real-time and single-cell quantification of DNA damage-dependent interactions, and can distinguish between direct protein–protein interactions, as opposed to those mediated by chromatin proximity. Using the UV-FLIM-FRET system, we show the dynamic changes in the interaction between poly(ADP-ribose) polymerase 1, amplified in liver cancer 1, X-ray repair cross-complementing protein 1 and tripartite motif containing 33 after DNA damage. This new set-up complements the toolset for studying DNA damage response by providing single-cell quantitative and dynamic information about protein–protein interactions at DNA damage sites.

INTRODUCTION

DNA damage is ubiquitous: our cells are constantly dealing with spontaneous lesions, environmental exposure to sun and smoke generates massive DNA damage, while chemotherapy is based on overloading highly proliferating cancer cells with DNA damage and replication stress. DNA damage elicits a complex response comprised of DNA damage sensing, chromatin remodelling, stress signalling and DNA repair, all of which are mediated through protein–protein interactions. Protein interactions are essential to ensure timely and precise recruitment of DNA damage response (DDR) factors to DNA damage sites.

Live cell fluorescence microscopy is a powerful tool to study the response of fluorescently tagged proteins to DNA damage. For example, laser microirradiation coupled with wide-field or confocal fluorescence microscopy has been broadly used for studying protein recruitment to the sites of laser-induced DNA damage (1–6). The efforts over the past two decades have yielded an increasingly detailed picture of the sequence in which DNA damage sensing factors, chromatin remodellers, and signalling and repair factors are recruited to and released from laser microirradiation sites (7–11). Recently, we developed a dual-channel simultaneous imaging approach to monitor and compare the recruitment kinetics of two proteins in response to DNA damage in the same cell (7).

Comparing the recruitment kinetics of proteins, however, does not allow conclusions about protein–protein interactions that facilitate their recruitment to DNA damage sites. Many DDR proteins are recruited to DNA damage sites in a poly(ADP-ribose) (PAR)-dependent manner (7,12–17). PAR is a post-translational protein modification generated primarily by poly(ADP-ribose) polymerase 1 (PARP1) upon binding to DNA strand breaks (18). PARP1 activation at DNA damage sites triggers chromatin relax-

---

*To whom correspondence should be addressed. Tel: +43 1427752811; Fax: +43 142779240; Email: dea.slade@univie.ac.at
Present address: Sébastien Herbert, Imaging Core Facility, University of Basel, Klingelbergstrasse 50/70, Basel, Switzerland.

ation due to rapid PARylation of histones leading to histone displacement (19–21). Additionally, PARylation triggers a wave of PAR-dependent recruitment of proteins to the site of DNA damage (7,12–17). Some proteins such as the chromatin remodeller amplified in liver cancer 1 (ALC1) and the single-strand break (SSB) repair scaffold protein X-ray repair cross-complementing protein 1 (XRCC1) were shown to directly bind PAR and interact with PARP1 in response to DNA damage (7,12,13,17,22,23). Unlike ALC1 and XRCC1, the chromatin remodellers CHD3 and CHD4 do not bind PAR and do not interact with PARP1 directly but require PAR-dependent chromatin relaxation for efficient recruitment to DNA damage sites (15,24,25). Therefore, a comprehensive understanding of protein networks at DNA damage sites necessitates a combination of kinetic information from protein recruitment studies and quantitative measurements of protein–protein interactions.

Here, we established a method that can provide at once a kinetic and a quantitative measurement of protein–protein interactions at a single-cell level. The method is based on measuring the interaction between fluorescently tagged proteins in response to localized DNA damage induced by a UV laser as a spot in the nucleus of live cells. Protein–protein interactions are measured based on Förster resonance energy transfer (FRET)—a proximity-dependent non-radiative energy transfer from a fluorescent donor to a spectrally overlapping acceptor upon excitation of the donor (26). FRET efficiency between a donor and an acceptor protein is determined based on fluorescence lifetime imaging (FLIM), which measures dynamic changes in the fluorescence lifetime of the donor fluorophore depending on its close proximity to the acceptor (27). Overall, the UV-FLIM-FRET system enables real-time measurement of fluorescence lifetimes at the site of UV laser-induced DNA damage and FRET-based quantification of protein–protein interactions at different time points after DNA damage. This system represents a unique tool to study and quantify dynamic protein–protein interactions at laser-induced DNA damage sites.

MATERIALS AND METHODS

Plasmids

mCherry-ALC1 and mEGFP-ALC1 were a kind gift from Sébastien Huet (15). mCherry-CHD4, mEGFP-CHD4 and LacI-GFP-nanobody construct were a kind gift from Gyula Timinszky (25). XRCC1 cDNA was transferred from pDONR221 to pDEST C-mEGFP. Proliferating cell nuclear antigen (PCNA) and tripartite motif containing 33 (TRIM33) were cloned into mCherry IRES puromycin vectors (Clontech) between AgeI and NotI for N-terminal tagging. PARP1 was cloned into mEGFP and mCherry IRES puromycin vectors (Clontech) between AgeI and NotI for N-terminal tagging. PARP1 E988K catalytically dead mutant, ALC1 D723A and XRCC1 R335A + K369A PAR binding-deficient mutants were generated by site-directed mutagenesis. mEGFP-PARG WT and mEGFP-PARG K409A mutant were generated as previously published (28).

Cell culture

U2OS WT and PARP1 KO cells (29) were maintained in Dulbecco's modified Eagle's medium (4.5 g/l glucose) (Sigma) supplemented with 10% fetal bovine serum (Sigma), 1% L-glutamine (Sigma) and 1% penicillin–streptomycin (Sigma) under 5% CO_2 at 37°C. U2OS-2B2 cells (25) were grown in the same conditions in medium supplemented with 25 μg/ml hygromycin. For all experiments, cells were seeded on 35-mm glass-bottom dishes (175 ± 15 μm; Greiner Bio-One) to achieve a confluence of 60–80% on the following day. Twenty-four hours after seeding, cells were pre-sensitized with 10 μM 5-bromo-2′-deoxyuridine (BrdU; Sigma) and transiently double transfected with combinations of mEGFP and mCherry plasmids using polyethylenimine (Polysciences). Twenty-four hours post-transfection, individual double-transfected cells with low and comparable expression levels were locally UV laser microirradiated.

Laser microirradiation

We equipped a commercially available time-correlated single photon counting (TCSPC) microscope (MicroTime 200, PicoQuant, Berlin) with a custom in-house built optical set-up to focus a 355 nm 20 kHz pulsed laser (iLASpulse; Roper) onto the sample. A single spot in the nucleus of a double-transfected cell was targeted with the 355 nm pulsed laser for 1 s to induce DNA damage. Intensity and duration of damage were controlled using an acousto-optic modulator (AOM): output 12.8 μW at the sample, 0.64 nJ per pulse (1.07 W peak power, 600 ps pulse width). FLIM was done before and 1–20 min after UV laser microirradiation. Alternatively, the cells were fixed with 4% paraformaldehyde 1–5 min after damage and prepared for immunofluorescence staining and acceptor photobleaching.

Fluorescence lifetime imaging

FLIM was performed on double-transfected cells showing low fluorescence intensity and comparable intensity levels of mEGFP and mCherry signals for the chosen acquisition parameters. Acquisitions were done sequentially, before and 1–20 min after UV laser microirradiation using a TCSPC set-up (MicroTime 200, PicoQuant, Berlin) equipped with single photon sensitive hybrid PMA detectors, a stable environmental control (37°C, 5% CO_2) and an objective heater system (Bioptechs). mEGFP excitation was achieved with a 485 nm pulsed laser diode (40 MHz repetition rate; pulse width ∼100 ps) and the laser output was set to ensure that detection rates in basal conditions remain below 400 000–800 000 counts per second (1–2% of the repetition rate) and detection rates at the damage site never exceed 5% of the repetition rate. With a pixel dwell time of 3.4 ms, this allowed the detection of up to 6000 photons per pixel. Emission was detected through a suitable interference bandpass filter (525/45 Semrock) and the confocal pinhole was fixed at 70 μm. A 60×/1.2 NA water immersion objective (UPlanSApo, Olympus) was laterally scanning the cells to generate 128 × 128 pixel 2D fluorescent lifetime maps with an effective pixel size of 0.156 μm. The 2D fluorescence lifetime maps were subsequently exported as binary files and

processed with SimFCS (Laboratory for Fluorescence Dynamics) to generate a phasor plot of the real versus imaginary parts of the Fourier transform components of the decay curve for each scanned voxel (30). Different positions on such a plot represent different lifetimes, which can be traced to a specific location on the image and highlighted. Phasors representing donor-only lifetime overlap with phasors representing donor lifetime in the presence of a non-interacting acceptor (marked in red in Figure 1D), while phasors representing shortened donor lifetime in the presence of an interacting acceptor (marked in yellow in Figure 1D) are separated along a FRET trajectory. The FRET efficiency (E) in % was read out from the software and calculated as $E = (1 - (\tau_{DA}/\tau_D)) \times 100$, where τ_{DA} represents the lifetime of an mEGFP-tagged protein (donor, D) in the presence of an mCherry-tagged protein (acceptor, A) and τ_D represents the lifetime of an mEGFP-tagged protein (donor, D) in the presence of an mCherry empty vector. Lifetimes and FRET efficiencies were directly read out from the phasor plot generated by SimFCS (30,31) after normalization to the lifetime of Atto488 (32). The sample size (N) for each experiment is listed in Supplementary Table S1 along with median values, 25th and 75th percentiles, and mean and confidence intervals. Detection rate-dependent correction of lifetimes (only for data in Supplementary Figure S3G and I) was performed based on $\tau_{corr} \approx \tau/(1 - P/4)$, where τ is the measured lifetime and P is the average number of photons in a given laser period (33). In our case, the laser repetition rate was 40 MHz such that a laser period amounts to 25 ns.

Antibodies

Rabbit anti-γH2AX (1:600; Bethyl A-300-081A), mouse anti-γH2AX (1:500; Millipore JBW301), mouse anti-CPD (1:500; Cosmo Bio NMDND001) and rabbit anti-PAR polyclonal (1:1000; Trevigen 4336-BPC-100) were used for immunofluorescence. Secondary Alexa Fluor® anti-rabbit 647 and anti-mouse 568 antibodies (Life Technologies) were used at 1:500 dilution. DAPI (5 mg/ml, Life Technologies) was used at a final concentration of 0.5 μg/ml to visualize nuclei.

Immunofluorescence

Individual cells were locally microirradiated as described earlier, fixed 1–5 min after damage with 4% formaldehyde in phosphate-buffered saline (PBS) for 10 min and washed twice in PBS for 5 min. Cells were subsequently permeabilized with 0.5% Triton–PBS for 8 min and washed three times with PBS. For anti-CPD staining, DNA was denatured with 0.5 M NaOH for 8 min at room temperature (RT) and washed three times with PBS. Cells were blocked for 30–60 min at RT with 3% bovine serum albumin–0.1% Tween–PBS. Coverslips were incubated in appropriate dilutions of primary antibodies for 1 h at RT, washed three times with PBS and incubated in 1:500 dilutions of secondary antibodies for 1 h at RT. After two washes with PBS, coverslips were incubated for 5–10 min in a 1:10 000 dilution of DAPI (Life Technologies) in PBS, washed once with PBS and once with water and overlaid with 60% glycerol + 20 mM Tris (pH 8).

Confocal microscopy and acceptor photobleaching

Images were acquired with LSM710 confocal microscope (Zeiss), mounted on Zeiss Axio Observer Z1 equipped with Plan-Apochromat 63×/1.4 oil immersion objective, a 405 nm laser diode (1.7 μW laser power at the sample), a 488 nm argon laser (2.8 μW), a 561 nm DPSS laser (23.2 μW) and a 633 nm HeNe laser (1.7 μW). Acceptor photobleaching was performed at a random nucleoplasmic region of undamaged cells or at an undamaged and damaged region of the nucleus in microirradiated cells. The damaged region was identified by mEGFP- and mCherry-tagged protein recruitment and γH2AX immunofluorescence staining. An mCherry-tagged protein (acceptor, A) was bleached with a high intensity (50% output) of the 561 nm DPSS laser for five iterations and a pixel dwell time of 25.21 μs per pixel. Images before and after acceptor photobleaching were acquired with Zen Black software (version 2.1, Zeiss) and processed with ImageJ by measuring the intensity of an mEGFP-tagged protein (donor, D) before (I_{DA}) and after (I_D) acceptor photobleaching. FRET efficiency (E) in % was calculated as $E = (1 - (I_{DA}/I_D)) \times 100$. The sample size ($N$) for each experiment is listed in Supplementary Table S2 along with median values, 25th and 75th percentiles, and mean and confidence intervals.

Spinning disc microscopy and UV laser microirradiation

U2OS-2B2 cells were seeded on four-chambered 35-mm glass-bottom dishes (175 ± 15 μm; Greiner Bio-One) and each well transfected as described earlier with the following plasmids: 100 ng LacI-GFP-nanobody, 100 ng mEGFP-tagged protein and 100 ng mCherry-tagged protein and pre-sensitized with 10 μM BrdU (Sigma) 24 h prior to imaging. Laser microirradiation was performed on a spinning disc confocal microscope (Visitron) equipped with a 355 nm pulsed laser (iLASpulse; Roper), an integrated point-scanning laser manipulation unit, a high-speed/high-resolution camera (EvolveEM512 EMCCD; Photometrics/Teledyne) and an environmental chamber to maintain physiological conditions (37°C, 5% CO_2). The samples were visualized with Visitron spinning disc (Yokogawa X1) set up on a Zeiss Axio Observer Z1-stand using an EC PlanNeoFluar 100×/1.30 NA oil iris objective lens, excited with a 488 nm–100 mW diode laser and a 561 nm–100 mW laser diode; equipment control and image capture were handled by Visiview software (Visitron). The 355-nm laser settings were as follows: 0.03 μJ per pulse (54 W peak power × 600 ps pulse width), 21 kHz repetition rate. Laser microirradiation across a nucleus was applied at 1 ms per pixel. Images were captured for 5 min in 500 ms intervals with an exposure time of 100 ms. Quantification of mCherry-tagged protein accumulation at the site of LacO-tethered mEGFP-tagged protein was done by measuring the fluorescence intensity of mCherry at the LacO site (I_{LacO}) normalized to the intensity of mCherry in a randomly chosen nucleoplasmic control region (I_C) of the same nucleus. The increase of mCherry intensity at the LacO site was calculated as % increase $= (1 - (I_C/I_{LacO})) \times 100$ before or 1, 2 and 5 min after UV laser microirradiation. The sample size (N) for each experiment is listed in Supplementary Table S3 along with me-

dian values, 25th and 75th percentiles, and mean and confidence intervals.

Statistical analysis

Error bars represent the 25th and 75th percentiles. Statistical significance was calculated using two-tailed Student's *t*-test. *P*-values <5% ($P < 0.05$) were considered statistically significant.

RESULTS

Validation of UV-FLIM-FRET as a new tool that combines UV laser damage with FLIM to quantify protein–protein interactions at DNA damage sites

To set up a system that allows measurement of protein–protein interactions at DNA damage sites at a single-cell level, we equipped the confocal FLIM system from Pico-Quant with a controllable pulsed 355 nm UV laser to induce highly localized DNA lesions within nuclei of mammalian cells (Supplementary Figure S1). TCSPC FLIM is a method that can robustly distinguish the lifetimes of different fluorophores in a fluorescence intensity-independent manner (27). Cells were co-transfected with an mEGFP-tagged protein donor and an mCherry-tagged protein acceptor, which constitute a spectrally suitable pair of fluorophores for FRET (34). FRET occurs only when donor and acceptor proteins are in close physical proximity up to 10 nm and if donor and acceptor dipole orientations are permitting energy transfer (35). FRET from the donor fluorophore (mEGFP) to the acceptor fluorophore (mCherry) is measured as a decrease in the fluorescence lifetime of the mEGFP donor (34). FLIM is not affected by fluorophore concentration, fluorescence intensity, photobleaching, spectral fluorophore crosstalk or differences in optical set-ups of different microscopes, and is thus robust and reproducible (27). Furthermore, FLIM measurements can be performed on a timescale suitable for DDR and with low phototoxicity making it a preferred method for live cell FRET studies. Transient overexpression of FRET protein pairs was chosen given that FLIM is independent of fluorophore concentration and that FRET quantification in live cells requires sufficiently high fluorescence intensity to reach desired photon counts in short acquisition times.

To confirm the suitability of the mEGFP–mCherry FRET pair and to determine the maximum FRET efficiency that can be measured with this system, we transfected mEGFP-empty and mCherry-empty vectors as a negative FRET control and mEGFP–mCherry fusion as a positive FRET control (28,36). TCSPC FLIM measurements were used to generate a map of fluorescent lifetime decay curves and the derived fluorescence lifetimes for each pixel in the scanned area (Supplementary Figure S2A and B). Routine FLIM data analysis involves fitting the fluorescent decay curves with a suitable decay kinetics model (27) (Supplementary Figure S2B). A double-exponential reconvolution fit yielded a median and maximum FRET efficiency of 21.4% and 26.3%, respectively, for the mEGFP–mCherry fusion (*N* = 23; Supplementary Figure S2C). To enable high-throughput analysis of multiple FLIM 'images' and

to circumvent curve fitting (which can also introduce uncertainties for complex decay dynamics), the time domain can be Fourier transformed and expressed as a phasor corresponding to each pixel of the FLIM map. These calculated phasors are typically represented in a so-called phasor plot, with a given decay curve represented as a single point in a plot of the real versus imaginary components of the calculated phasor, corresponding to the real and imaginary Fourier components of the fluorescence lifetime decay curve (30) (Figure 1D, and Supplementary Figure S2E and K). The phasor approach is suitable for studying FRET-induced lifetime changes of donor fluorophores with complex, multi-exponential decay dynamics without prior assumption of a model for the decay dynamics (31).

Phasor analysis using the SimFCS software (Globals Software) allows the experimenter to mark a cluster of phasors on the phasor plot, which automatically highlights the corresponding pixels on the FLIM image (Figure 1D, and Supplementary Figure S2D and J). To establish the positions of phasors, we measured Atto488 as a calibration sample as well as untransfected cells to determine the background. In cells transfected with mEGFP-empty and mCherry-empty vectors (negative control) and mEGFP–mCherry fusion (positive control), phasors for the unquenched donor (mEGFP-empty), quenched donor (mEGFP in mEGFP–mCherry fusion) and background are marked using the SimFCS software, which automatically calculates a FRET trajectory and displays the FRET efficiency of phasors located along this curve. Maximum and median FRET efficiency measured for the mEGFP–mCherry fusion was 27.7% and 18.4% (Supplementary Figure S2F). Given that the mEGFP–mCherry fusion represents ideal proximity for FRET, we conclude that the maximum FRET efficiency that can be measured with our system is 28%, provided that the same amounts of donor and acceptor are available.

In the UV-FLIM-FRET set-up, cells were pre-sensitized with the nucleoside analogue BrdU, which upon UV laser microirradiation yields a complex mixture of DNA lesions including CPDs, oxidative damage, SSBs and double-strand breaks (DSBs) (5,37–39). UV laser microirradiation was applied as a single spot in the nucleus (Figure 1B). Induction of DSBs, SSBs and CPDs was verified by immunofluorescence staining with an antibody against γH2AX, PAR and CPDs, respectively. Five minutes after UV laser microirradiation, a strong signal of γH2AX, PAR and CPDs was detectable within a small region of the nucleus (Figure 1F). FLIM images were obtained before UV laser damage and at different time points after damage. Phasor analysis allowed us to distinguish changes in the donor (mEGFP) lifetime in the presence of an acceptor at a laser-induced damage site as opposed to the rest of the nucleus (Figure 1D and Supplementary Figure S2G–L).

To determine the suitability of SimFCS for FRET analysis at DNA damage sites in the UV-FLIM system, we compared curve fitting and the phasor approach in a small sample set of mEGFP-PARP1 + mCherry-empty (negative control) and mEGFP-PARP1 + mCherry-ALC1 before damage, and 1 and 2 min after DNA damage (Supplementary Figure S2G–L). Curve fitting requires multiple steps of global double-exponential reconvolution fitting, fitting in-
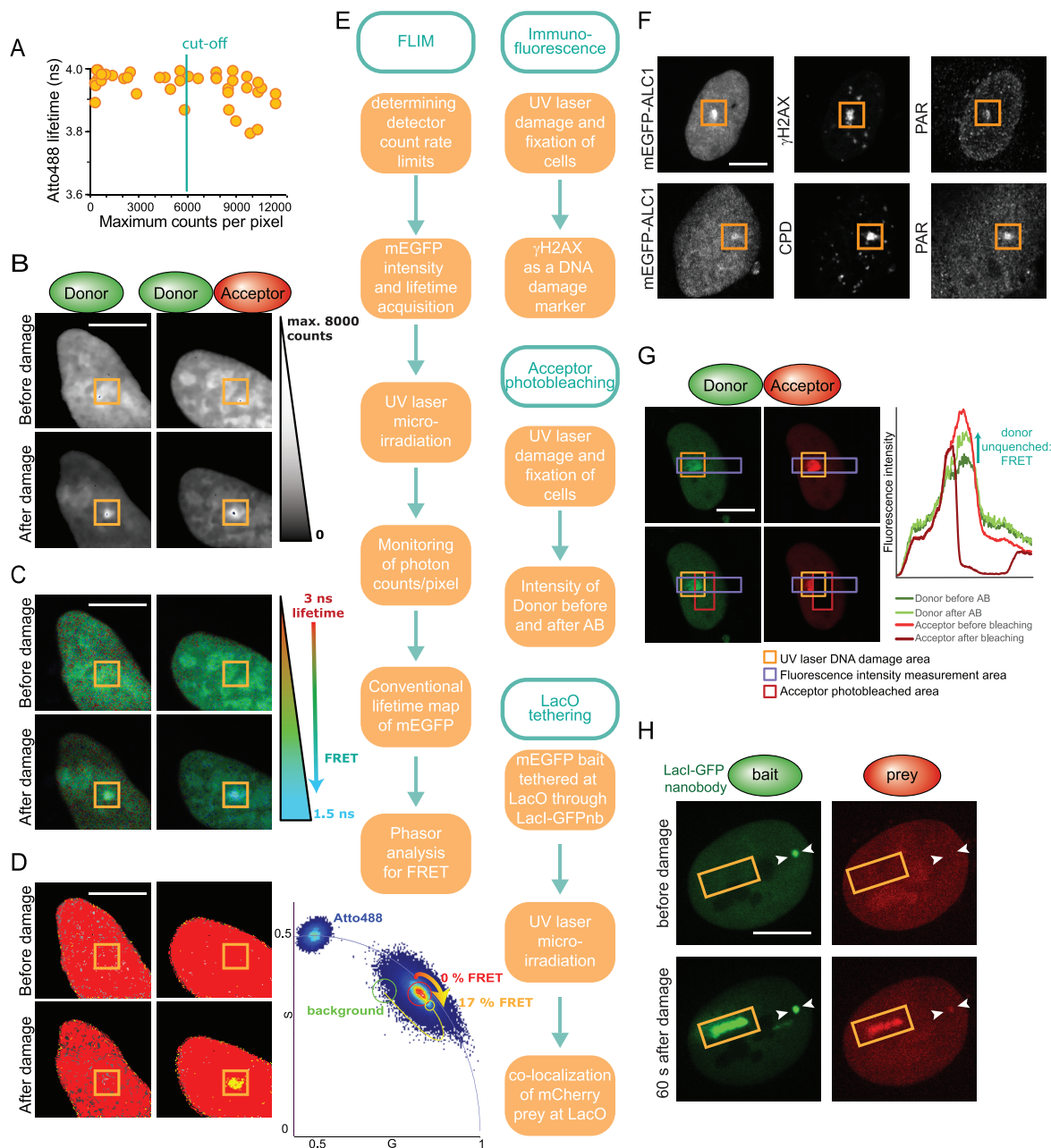
Figure 1. The UV-FLIM-FRET system and the experimental outline for analysing interaction between mEGFP- and mCherry-tagged proteins before and after UV laser-induced microirradiation by three independent methods. (**A**) Lifetime of Atto488 at increasing excitation power until detector pile-up artefacts became apparent as a drop in measured lifetimes. (**B**) Live U2OS cells transiently co-transfected with mEGFP-tagged protein (donor) and either with mCherry-empty vector or with mCherry-tagged interaction partner (acceptor) and imaged before and after inducing DNA damage. Sites of laser damage are visible by increased photon count numbers caused by rapid protein recruitment to the site of laser microirradiation (indicated with an orange box within the nucleus). (**C**) Fluorescence lifetime decay curves plotted as a pixel-by-pixel heatmap of measured mEGFP lifetimes scaled from red (3 ns lifetime) to light blue (1.5 ns lifetime) to visualize changes in the lifetime of the donor in the presence of an acceptor at sites of UV laser microirradiation (orange boxes) or in the rest of the nucleus. (**D**) Phasors representing background fluorescence (marked with a green circle on the phasor plot), donor-only lifetime (marked with a red circle on the phasor plot, corresponding regions where no FRET occurs are highlighted in red on the FLIM image of the cell) and phasors representing shortened donor lifetime in the presence of an interacting acceptor (marked with a yellow circle on the phasor plot, corresponding regions of FRET on the FLIM map highlighted in yellow) are separated along a FRET trajectory (marked with a yellow line on the phasor plot). (**E**) Experimental outline for FLIM, immunofluorescence, acceptor photobleaching and LacO tethering. (**F**) mEGFP-ALC transfected cells were fixed after damage and damage sites identified by the accumulation of mEGFP-ALC1 and co-localization with γH2AX, PAR and cyclobutane pyrimidine dimers (CPDs) detected by immunofluorescence staining. (**G**) Acceptor photobleaching on cells fixed after UV laser damage. Damage sites were identified by γH2AX immunofluorescence staining and by increased fluorescence intensity due to protein accumulation at the damage site (marked by an orange square). Acceptor was bleached in a region marked with a red square and the intensity of mEGFP measured across a region marked with a purple square before and after bleaching the acceptor. (**H**) Accumulation of mCherry-tagged prey at the LacO site (white arrow) in live U2OS-2B2 cells was observed in a fluorescence three-hybrid assay when the prey was able to interact with the mEGFP-tagged bait tethered at LacO with a LacI-GFP nanobody. All scale bars indicate 10 μm.

side a DNA damage region of interest (ROI) and in an inverted ROI outside of the damage site for each condition. The two approaches yielded comparable results, demonstrating that they are both suitable for the measurement of interaction at the site of damage compared to the rest of the nucleus (Supplementary Figure S2G–L). The phasor approach was used for the analysis of all further experiments as it involves fewer steps and allows analysis of multiple cells simultaneously, without selecting different ROIs, and independently of curve fitting.

One of the caveats of FLIM is detector pile-up effects caused by the unavoidable dead time of a detector after photon detection (27,40). As this can result in artificially lowered lifetimes, it is recommended to keep the photon detection rate below 10% of the excitation repetition rate (27). This is particularly relevant for DDR experiments as the strong recruitment of many DDR proteins to laser damage sites results in an increase of photon counts at the damage site compared to the rest of the nucleus. In order to validate the detection limitation range for the UV-FLIM-FRET imaging configuration, we measured the lifetime of Atto488, which is highly photostable and has a monoexponential decay (32). Increasing the laser excitation power for consecutive measurements until the photon count limits of the detectors were reached allowed us to establish a threshold of 8000 counts per pixel below which the measured lifetime remained comparable to the expected lifetime (4 ns) (32) (Figure 1A). Calculating a false-positive FRET efficiency based on these lifetimes showed that below 6000 counts the rate of false-positive FRET remained negligible (Supplementary Figure S3A). We applied similar conditions to measure the lifetime of mEGFP-empty in the presence of mCherry-empty at an increasing number of counts per pixel and found that, similar to Atto488, the rate of false-positive FRET was negligible below 6000 counts per pixel for mEGFP (Supplementary Figure S3A). Six thousand counts per pixel with the UV-FLIM-FRET imaging settings correspond to a detection rate at 5% of the excitation laser repetition rate. For all further experiments, we chose excitation settings that ensured the detection rate did not exceed 5% and the maximum mEGFP counts per pixel did not exceed 6000. As a quality control, the maximum number of counts per pixel at the damage site was plotted against the calculated FRET efficiency for each cell (Supplementary Figure S3). This analysis confirmed no influence of the increase in photon counts on FRET efficiency with the exception of mEGFP-ALC1 + mCherry-TRIM33 (Supplementary Figure S3G).

Local spikes in the count rate at detection rates below 10% were reported to affect the measured lifetime and require mathematical corrections (33). To test whether such a correction should be applied to our measurements, we used the dataset where we detected a correlation between count rate and FRET efficiency (ALC1 + TRIM33; Supplementary Figure S3G). The median difference between the measured lifetimes and the corrected lifetimes was below 0.6% and the single most affected data point had a difference of <1.5% (Supplementary Figure S3I). Thus, within our constrained imaging settings, none of the FRET data were skewed by high count rates and additional correction was not necessary. Furthermore, to ensure that loss of FRET is

a biological effect and not an artefact caused by the lack of acceptor molecules within the sample, we routinely plotted the mCherry counts against the FRET efficiency for all experiments to ensure consistency in the relative abundance of mCherry (Supplementary Figure S3).

Given that lifetimes of fluorophores are highly sensitive to changes in environmental conditions such as pH or to changes of the biochemical environment within the cell, FLIM-FRET experiments need to include a control to assess FRET-independent variability of the donor lifetime in the absence of an acceptor (27). To this end, in all our experiments we used a donor-only control in which the lifetime of mEGFP-tagged proteins was measured in the presence of the mCherry-empty vector to ensure that laser microirradiation and subsequent cellular responses do not trigger changes in the lifetime of mEGFP. The stability of measured mEGFP lifetime in our experimental set-up is depicted in a representative sample cell (Figure 1B–D, left panels, and Supplementary Figure S2G and J, left panels) and routinely quantified throughout our experiments as a negative control (plotted as dark grey).

To validate the suitability of the UV-FLIM-FRET system for measuring protein–protein interactions at DNA damage sites, we used two additional approaches. First, we performed acceptor photobleaching on UV laser-damaged fixed cells and measured the intensity of the donor (mEGFP-tagged protein) before and after bleaching the acceptor (mCherry-tagged protein). Increase in donor intensity after bleaching the acceptor, referred to as donor unquenching, indicates interaction between the donor and the acceptor (41) (Figure 1G). Second, we validated our results independent of FRET measurements using a fluorescence three-hybrid assay (25,42). In this assay, an mEGFP-tagged protein bait is tethered to a LacO array through a LacI-GFP-nanobody. Accumulation of an mCherry-tagged protein prey at the LacO site indicates interaction between the protein pair (Figure 1H). This assay was used to distinguish between PAR-dependent recruitment of DDR proteins to the site of DNA damage resulting from PAR binding or from chromatin relaxation induced by PAR (25). It robustly and sensitively discriminates protein–protein interaction that is independent of DNA damage (accumulation of prey at LacO-tethered bait in basal conditions) from DNA damage-dependent interaction (accumulation of prey at LacO-tethered bait after DNA damage) and co-recruitment to the damage site without interaction (no accumulation of prey at LacO).

DNA damage-induced transient interaction between PARP1 and ALC1

For proof-of-concept experiments, we used well-characterized pairs of DNA damage-dependent interactors, PARP1 and ALC1 (Figure 2) and PARP1 and XRCC1 (Figure 3). The chromatin remodeller ALC1 is recruited to DNA damage sites upon PAR binding and promotes chromatin relaxation (12,13,15). PAR binding triggers a conformational change that releases ALC1 from auto-inhibited to ATPase active state (22,23). To test whether UV-FLIM-FRET can detect DNA damage-induced interaction between PARP1 and ALC1, we
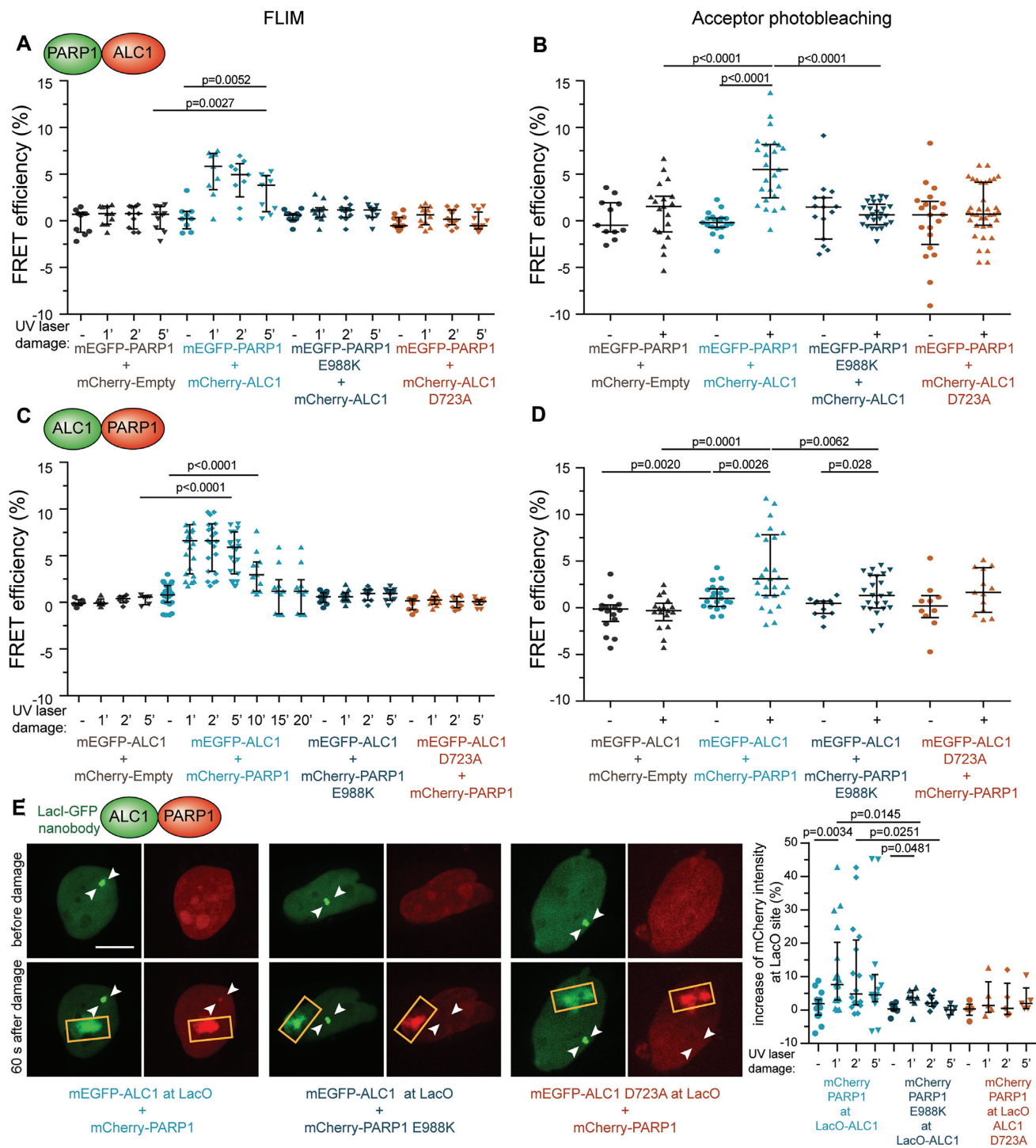
Figure 2. DNA damage- and PAR-dependent transient interaction between ALC1 and PARP1. (**A**) DNA damage-dependent FLIM-FRET efficiencies (%) between mEGFP-PARP1 and mCherry-ALC1 (light blue points). No FRET was measured in the absence of an acceptor (grey points) or when PARP1 activity and PAR binding were abrogated (dark blue and orange points). (**B**) FRET measured by acceptor photobleaching for the same FRET pairs as in (A). (**C**) Switch-tag FLIM-FRET. (**D**) Switch-tag FRET measured by acceptor photobleaching. (**E**) Fluorescence three-hybrid assay shows damage-dependent accumulation of mCherry-PARP1 at the LacO dot (white arrow) where mEGFP-ALC1 was tethered (left panels and light blue points) but not where the PAR binding-deficient mEGFP-ALC1 D723A was tethered (right panels and orange points). mCherry-PARP1 catalytic dead mutant E988K does not accumulate at the mEGFP-ALC1 dot (middle panels and dark blue points). Scale bar indicates 10 μm. The scatter plots show individual quantifications; bars indicate median, and 25th and 75th percentiles (all values listed in Supplementary Tables S1–S3).
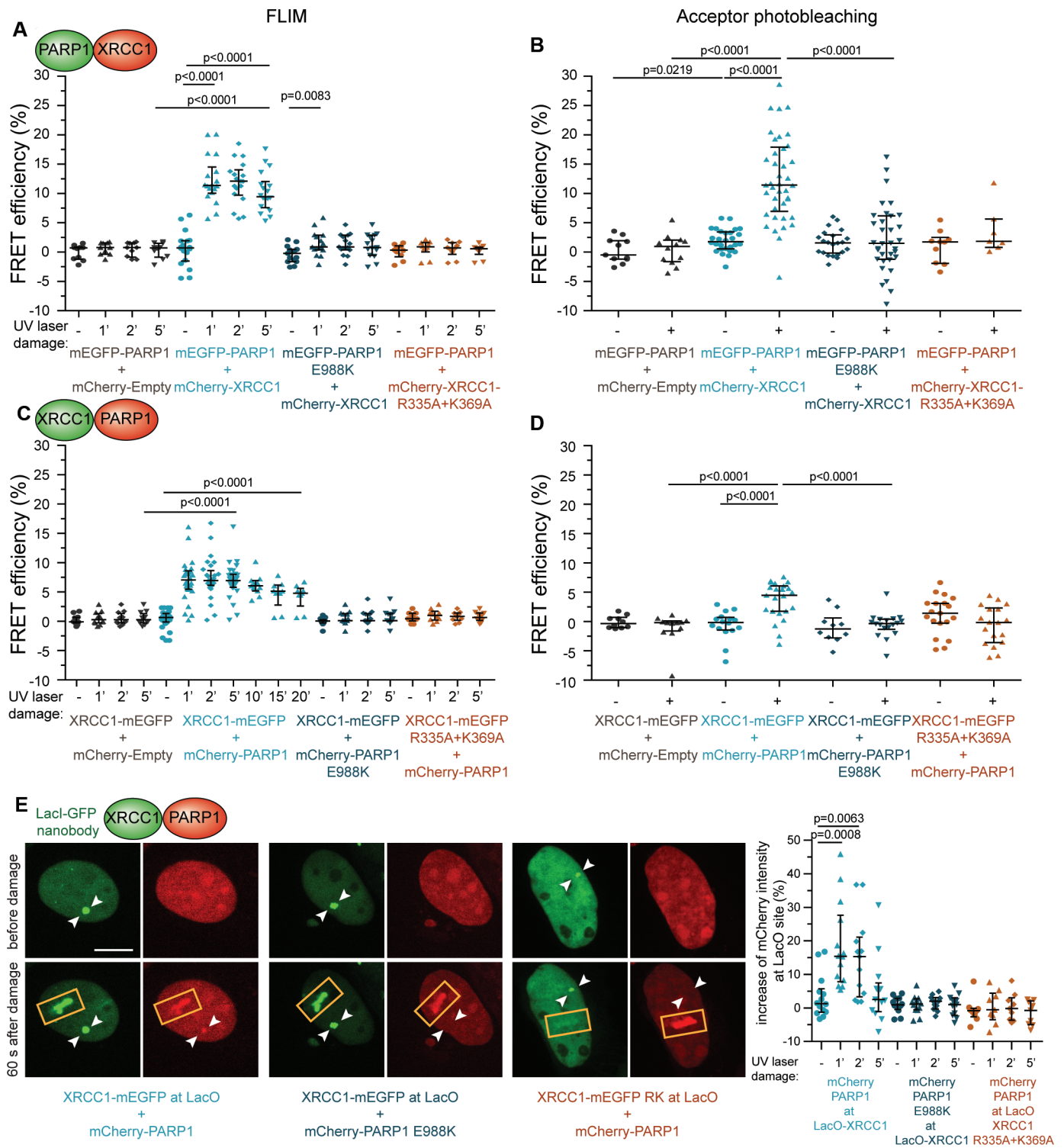
Figure 3. DNA damage- and PAR-dependent persistent interaction between XRCC1 and PARP1. (**A**) DNA damage-dependent FLIM-FRET efficiencies (%) between mEGFP-PARP1 and mCherry-XRCC1 (light blue points). No FRET was measured in the absence of an acceptor (grey points) or when PARP1 activity and PAR binding were abrogated (dark blue and orange points). (**B**) FRET measured by acceptor photobleaching for the same FRET pairs as in (A). (**C**) Switch-tag FLIM-FRET. (**D**) Switch-tag FRET measured by acceptor photobleaching. (**E**) Fluorescence three-hybrid assay shows damage-dependent accumulation of mCherry-PARP1 at the LacO dot (white arrow) where XRCC1-mEGFP was tethered (left panels and light blue points) but not where PAR binding-deficient XRCC1-mEGFP R335A K369A was tethered (right panels and orange points). mCherry-PARP1 catalytic dead mutant E988K does not accumulate at the XRCC1-mEGFP dot (middle panels and dark blue points). Scale bar indicates 10 μm. All scatter plots show individual quantifications; bars indicate median, and 25th and 75th percentiles (all values listed in Supplementary Tables S1–S3).

transfected mEGFP-PARP1 and mCherry-ALC1 or a switch-tag combination into U2OS PARP1 KO cells (29) (Figure 2). U2OS PARP1 KO cells were used in all further FRET experiments that involved PARP1 as a donor or an acceptor to exclude the influence of endogenous PARP1.

UV-FLIM-FRET revealed no interaction between mEGFP-PARP1 and mCherry-ALC1 under basal conditions but strong interaction at UV laser-induced DNA damage sites (Figure 2A). Quantification based on phasor analysis revealed maximum interaction 1 min after damage (median FRET efficiency = 5.8%) followed by a subsequent decline (4.9% and 3.8%, 2 and 5 min after damage, respectively) (Figure 2A). The interaction was limited to the DNA damage site, as FRET was not detected in undamaged regions of the nucleus (Supplementary Figure S6A). Switching donor and acceptor tags resulted in comparable FRET measurements; mEGFP-ALC1 and mCherry-PARP1 reached maximum interaction 1 min after damage (median FRET efficiency = 6.6%) followed by a decline of interaction (5.9%, 2.9% and 1.2%, 5, 10 and 15 min after damage, respectively) (Figure 2C). This confirmed that UV-FLIM-FRET measurements are independent of the fluorophore type.

To test whether PARP1–ALC1 interaction is PAR dependent, we used the PARP1 catalytic dead mutant E988K, which is recruited to laser damage sites with similar intensity but slightly delayed kinetics and prolonged retention compared to wild-type PARP1 (6,7). Additionally, we used the ALC1 macrodomain mutant D723A, which cannot bind PAR and shows diminished recruitment to laser damage sites (12,13). In line with the published data, UV-FLIM-FRET showed loss of interaction between ALC1 and the PARP1 catalytic dead mutant E988K as well as the ALC1 macrodomain mutant D723A and PARP1 wild type (Figure 2A and C).

The UV-FLIM-FRET results were corroborated by acceptor photobleaching (Figure 2B and D) and the fluorescence three-hybrid assay (Figure 2E). Acceptor photobleaching experiments showed an increase in interaction at laser damage sites (5.5% and 3.1% median FRET efficiency), which was lost with the catalytic dead PARP1 or the PAR binding-deficient ALC1 (Figure 2B and D). Furthermore, the fluorescence three-hybrid assay did not detect interaction between mEGFP-ALC1 and mCherry-PARP1 in basal conditions but showed laser damage-induced accumulation of mCherry-PARP1 at mEGFP-ALC1 tethered to the LacI-GFP-LacO array, as previously published (Figure 2E) (25). PARP1 and ALC1 mutants showed loss of interaction at the LacO array, in accordance with the UV-FLIM-FRET and acceptor photobleaching results, indicating damage-dependent activation of PARP1 and PAR-mediated interaction with ALC1 (Figure 2E).

The fluorescence three-hybrid assay detected PARP1–ALC1 interaction at the LacO array away from the damage site. In the fluorescence three-hybrid assay, bait tethering at the LacO array (e.g. mEGFP-ALC1) facilitates accumulation of a potential interactor (e.g. mCherry-PARP1), which makes this method particularly suitable for detecting transient or weak interactions. Although less sensitive than the fluorescence three-hybrid assay, UV-FLIM-FRET

allows quantification of protein–protein interaction at high spatial and temporal resolution.

DNA damage-induced persistent interaction between PARP1 and XRCC1

The scaffold protein XRCC1 binds PAR generated by PARP1 or PARP2 through a phospho-binding pocket in its BRCT domain (17,43). Another basic patch on the opposite side of the BRCT domain is critical for DNA binding (44). XRCC1 recruitment to DNA damage sites is PAR dependent (17,45), while its retention at DNA damage sites is dependent on its DNA binding ability (44). UV-FLIM-FRET measurements showed no interaction between mEGFP-PARP1 and mCherry-XRCC1 in basal conditions but strong DNA damage-induced interaction with 11.4% median FRET efficiency 1 min after laser damage (Figure 3A). PARP1–XRCC1 interaction persisted 2 min after damage (12.1%) and was slightly reduced 5 min after damage (9.4%). PARP1–XRCC1 interaction was limited to the site of damage with no interaction measured in the rest of the nucleus (Supplementary Figure S6C and D). Switching donor and acceptor protein confirmed strong interaction between XRCC1-mEGFP and mCherry-PARP1 at the damage site with a median FRET efficiency of 7% 1–5 min after damage, reduced to 6%, 5% and 4.7% 10, 15 and 20 min after damage, respectively (Figure 3C). The decrease in interaction between PARP1 and XRCC1 was delayed and more gradual compared to PARP1 and ALC1, suggesting that the interaction between PARP1 and XRCC1 is more persistent (Figures 2 and 3).

The interaction was abolished with the PARP1 catalytic dead mutant E988K (Figure 3A and C). To further examine the PAR binding dependence of the interaction, we paired PARP1 with the XRCC1 PAR binding-deficient mutant R335A K369A (17), which also resulted in a striking loss of interaction (Figure 3A and C).

Acceptor photobleaching yielded comparable results with strong damage-dependent interaction (FRET efficiency = 11.4% and 4.4%) (Figure 3B and D). The interaction was again abrogated by the catalytic dead PARP1 or the PAR binding-deficient XRCC1 (Figure 3B and D). The fluorescence three-hybrid assay did not detect interaction between XRCC1 and PARP1 at the LacO array in basal conditions but revealed strong colocalization in response to laser microirradiation, which was dependent on the PARP1 catalytic activity and the PAR binding ability of XRCC1 (Figure 3E).

In summary, UV-FLIM-FRET revealed a strong but transient DNA damage- and PAR-dependent interaction between PARP1 and ALC1, and a more persistent interaction between PARP1 and XRCC1 at DNA damage sites. The UV-FLIM-FRET set-up is thus highly suitable for quantification of protein–protein interactions in response to DNA damage with high temporal resolution.

Interaction between ALC1 and XRCC1 increases at DNA damage sites in a PAR binding-dependent fashion

ALC1 and XRCC1 were shown to co-immunoprecipitate in a PAR-dependent manner under basal conditions, with

a slight reduction after H_2O_2 treatment ([12]). UV-FLIM-FRET confirmed strong basal interaction between XRCC1-mEGFP and mCherry-ALC1 (FRET of 6%) or between mEGFP-ALC1 and mCherry-XRCC1 (FRET of 6.8%) (Figure [4]A and C). Surprisingly, FRET between XRCC1 and ALC1 increased after laser damage to 13–15% after 1 min and continued to rise to 20–22% 5 min after damage, but this strong increase was limited to the site of damage (Figure [4]A and C, and Supplementary Figure S6E and F). PAR binding mutations of ALC1 or XRCC1 did not impair their interaction under basal conditions but almost completely abrogated DNA damage-induced increase in FRET at the damage site (Figure [4]A and C, and Supplementary Figure S6E and F). Acceptor photobleaching confirmed PAR-independent interaction in basal conditions (2–3% FRET efficiency) and PAR-dependent increase after laser damage (4–5% FRET efficiency) (Figure [4]B and D). In addition, the fluorescence three-hybrid assay showed weak interaction between ALC1 and XRCC1 at the LacO array independent of DNA damage or PAR binding, followed by an increased co-accumulation at the LacO site after laser microirradiation only when PAR binding ability of both proteins remained intact (Figure [4]E). Overall, ALC1 and XRCC1 can interact independent of DNA damage but show a strong increase in interaction after DNA damage, which is dependent on PAR binding.

Interaction between ALC1 and TRIM33 at DNA damage sites is dependent on ALC1 PAR binding

TRIM33, also known as TIF1-γ, is a transcriptional repressor with ubiquitin ligase activity and a chromatin binding PHD finger-bromodomain ([46]). TRIM33 exhibits PAR-dependent recruitment to laser-induced DNA damage sites without directly binding PAR ([14]). Instead, recruitment of TRIM33 was shown to be mediated by interaction with the ALC1 macrodomain and dependent on ALC1 PAR binding ([14]). In basal conditions, FLIM measurements revealed weak interaction between mEGFP-ALC1 and mCherry-TRIM33 (4% median FRET efficiency) but no interaction with acceptor photobleaching (−0.2% median FRET efficiency) (Figure [5]A and B). UV-FLIM-FRET and acceptor photobleaching both showed increased interaction between ALC1 and TRIM33 at the damage site of microirradiated cells (7.7% and 2.2% median FRET efficiency, respectively) (Figure [5]A and B) and damage-independent interaction in the rest of the nucleus (Supplementary Figure S7A). With the ALC1 PAR binding mutant, the interaction was completely abrogated both before and after laser damage (Figure [5]A and B). The discrepancy between FLIM and acceptor photobleaching may stem from fixation artefacts. Cell fixation can result in reduced fluorescence signal and may explain why FRET efficiencies measured by acceptor photobleaching are lower than the more robust and intensity-independent live cell FLIM-FRET results. Fluorescence three-hybrid experiments confirmed weak PAR binding-dependent colocalization of mCherry-TRIM33 with mEGFP-ALC1 in basal conditions with a slight increase after damage (Figure [5]C). Moreover, severely reduced recruitment of TRIM33 to the laser damage site when combined with the PAR binding-deficient ALC1 indi-

cates that ALC1 activation is necessary to facilitate recruitment of TRIM33 (Figure [5]C). Taken together, these results show that live cell FLIM-FRET is the method of choice particularly in cases where weak interactions can be lost upon cell fixation or when small changes may not be easily quantifiable by intensity-based methods.

PARG and PCNA interact independent of DNA damage

Poly(ADP-ribose) glycohydrolase (PARG), the enzyme responsible for removal of PAR by cleaving ADP-ribose ([47]), is recruited to the sites of laser microirradiation in a PAR- and PCNA-dependent manner ([1,7,28]). PARG has a non-canonical PCNA-interacting peptide (PIP) box in which a single point mutation, K409A, abrogated interaction with PCNA ([28]). We confirmed strong and PIP box-dependent interaction between mEGFP-PARG and mCherry-PCNA in basal conditions using FLIM (15.8% median FRET efficiency), acceptor photobleaching (8.4% median FRET efficiency) and fluorescence three-hybrid assay (Supplementary Figure S4). Significantly, PARG–PCNA interaction was unaffected by UV laser damage (Supplementary Figure S7B). A slight increase in interaction between PARG K409A and PCNA after damage in acceptor photobleaching experiments may be due to fixation artefacts, given that this was not observed in UV-FLIM-FRET and fluorescence three-hybrid assays. Of note, both PCNA and PARG are strongly recruited to DNA damage sites and yet do not show stronger interaction compared to basal conditions, suggesting that an increase in protein concentration at the damage site due to protein recruitment does not lead to a false-positive increase in FRET measurements.

UV-FLIM-FRET does not detect indirect chromatin-mediated interactions

FRET between two proteins in a locally crowded environment such as DNA damage sites could be due to their chromatin proximity. To test whether UV-FLIM-FRET detects such false-positive FRET, we investigated interaction between PARP1 and CHD4 at DNA damage sites (Supplementary Figure S5) and in nuclear regions away from the damage site (Supplementary Figure S7C and D). The chromatin remodeller CHD4 is recruited to DNA damage sites in a PAR-dependent manner but does not interact with PARP1 or PAR directly ([25,48,49]). UV-FLIM-FRET did not detect interaction between CHD4 and PARP1 either in basal conditions or after laser microirradiation (Supplementary Figure S5A and B), which was confirmed by the fluorescence three-hybrid assay (Supplementary Figure S5C) ([25]). CHD4 recruitment to laser damage sites was reduced in the presence of the PARP1 catalytic dead mutant E988K, confirming that CHD4 recruitment is PAR dependent (Supplementary Figure S5C) ([48,49]). Taken together, UV-FLIM-FRET robustly distinguishes chromatin-mediated proximity, as is the case of PARP1 and CHD4, from direct interaction.

DISCUSSION

DDR is fast, dynamic and complex. DNA lesions are the sites of intense trafficking of proteins that sense DNA dam-
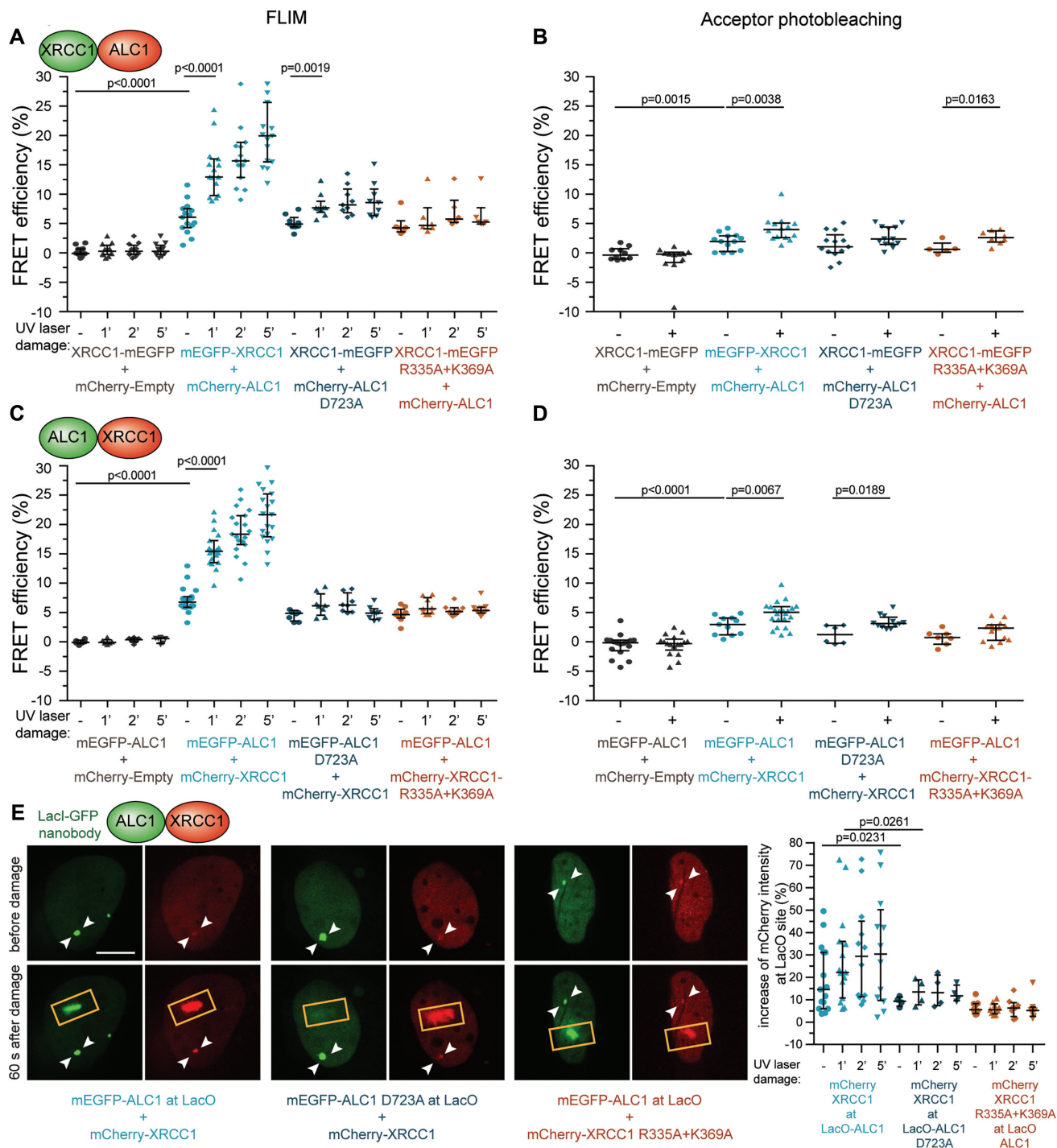
Figure 4. DNA damage- and PAR-dependent increase of interaction between ALC1 and XRCC1. (**A**) FLIM-FRET efficiencies (%) between XRCC1-mEGFP and mCherry-ALC1 (light blue points). No FRET was measured in the absence of an acceptor (grey points). PAR binding-deficient mutants (dark blue and orange points) do not show DNA damage-induced increase in interaction. (**B**) FRET measured by acceptor photobleaching for the same FRET pairs as in (A). (**C**) Switch-tag FLIM-FRET. (**D**) Switch-tag FRET measured by acceptor photobleaching. (**E**) Fluorescence three-hybrid assay shows damage-dependent increase of accumulation of mCherry-XRCC1 at the LacO dot (white arrow) where mEGFP-ALC1 was tethered (left panels and light blue points) but only weak accumulation without damage-dependent increase where PAR binding-deficient mEGFP-ALC1 D723A was tethered (middle panels and dark blue points). PAR binding-deficient mCherry-XRCC1 R335A K369A does not accumulate at the mEGFP-ALC1 dot (right panels and orange points). Scale bar indicates 10 μm. The scatter plots show individual quantifications; bars indicate median, and 25th and 75th percentiles (all values listed in Supplementary Tables S1–S3).
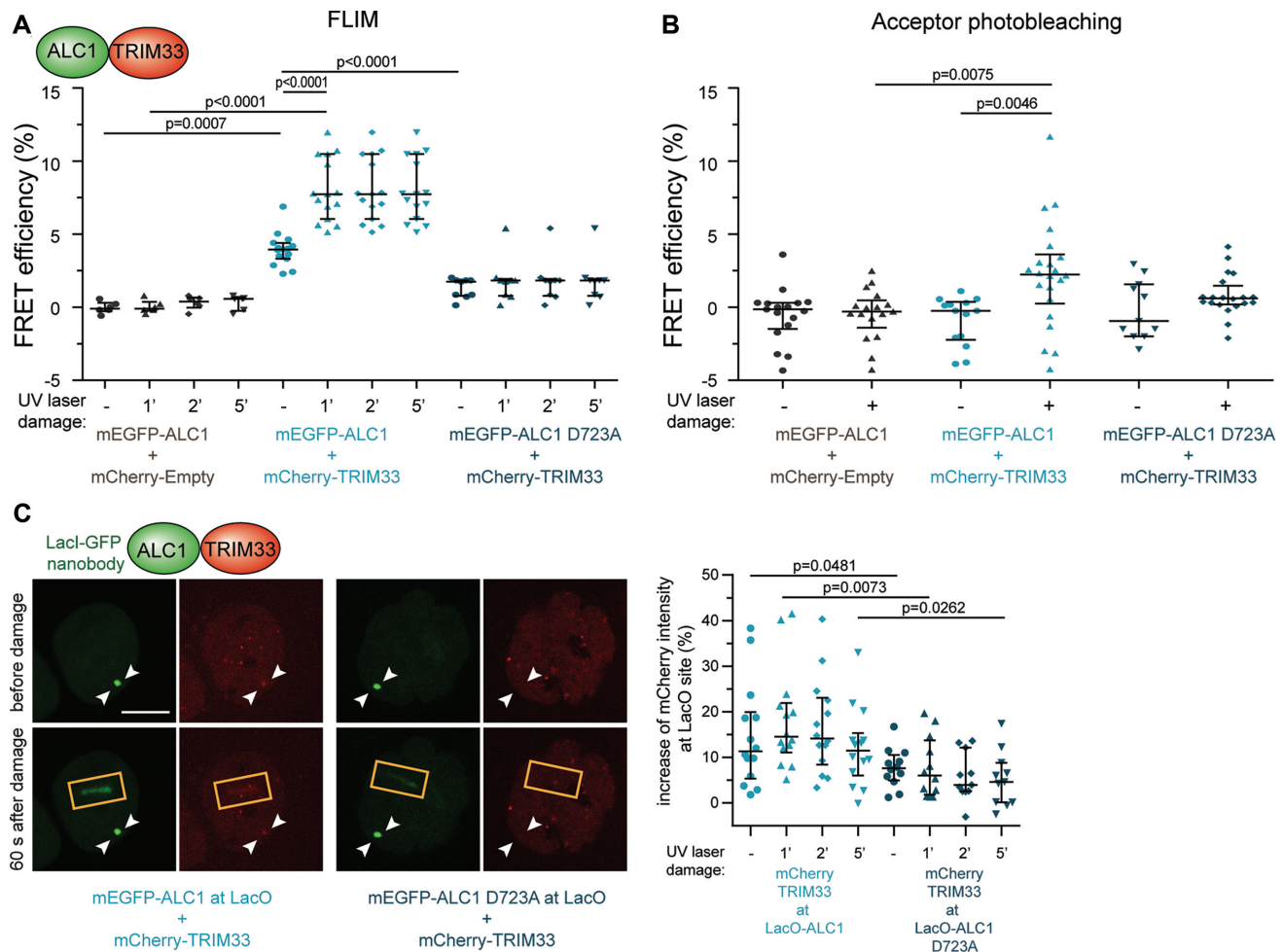
Figure 5. DNA damage- and PAR-dependent increase of interaction between ALC1 and TRIM33. (**A**) FLIM-FRET efficiencies (%) between mEGFP-ALC1 and mCherry-TRIM33 (light blue points). No FRET was measured in the absence of an acceptor (grey points) or for the PAR binding-deficient ALC1 (dark blue points). (**B**) FRET measured by acceptor photobleaching for the same FRET pairs as in (A). (**C**) Fluorescence three-hybrid assay shows damage-dependent increase of accumulation of mCherry-TRIM33 at the LacO dot (white arrow) where mEGFP-ALC1 was tethered (light blue points) but not where PAR binding-deficient mEGFP-ALC1 D723A was tethered (dark blue points). Scale bar indicates 10 μm. The scatter plots show individual quantifications; bars indicate median, and 25th and 75th percentiles (all values listed in Supplementary Tables S1–S3).

age, remodel chromatin and communicate the stress signal to DNA repair or transcription machinery. Protein–protein interactions dictate the dynamics of DDR by coordinating protein trafficking at DNA lesions. In this study, we established UV-FLIM-FRET as a new tool to study and quantify the dynamics of protein–protein interactions at a single-cell level using time-resolved fluorescence microscopy. We built the system by coupling a pulsed UV laser with a commercially available FLIM microscope. DDR proteins are labelled with two different fluorophores, mEGFP (donor fluorophore) and mCherry (acceptor fluorophore). Interaction between donor and acceptor leads to a non-radiative energy transfer phenomenon called FRET. FRET causes a reduction in fluorescence lifetime, which is measured by FLIM. After applying DNA damage with the UV laser at a defined region within the cell, the UV-FLIM-FRET system can measure the immediate effect of UV laser-induced DNA damage on the interaction of protein pairs in live cell.

Conventional methods for studying the dynamics of protein–protein interactions in DDR such as co-

immunoprecipitation, proximity-based biotinylation or cross-linking followed by mass spectrometry analysis do not allow the analysis of protein–protein interactions at a single-cell level and in exact spatial relation to the DNA damage site (50–52). Protein colocalization studies based on conventional fluorescence microscopy (at a single-cell level) or chromatin immunoprecipitation (genome-wide) cannot be used as a readout for direct protein–protein binding (53). Although colocalization correlation coefficients are becoming more reliable with the development of different super-resolution and 3D imaging techniques (53), cell fixation can introduce artefacts and does not allow dynamic measurements. Bimolecular fluorescence complementation (BiFC) detects protein–protein interaction based on the reconstitution of a fluorescent protein from complementary fragments fused to two proteins of interest in live cells. However, BiFC may detect indirect protein–protein interaction and is not suitable for analysing transient interactions (53). Proximity ligation assay is suitable for *in situ* protein–protein interaction studies but requires the

design of specific probes, which limits versatility and can lead to artefacts (54). Furthermore, methods that rely on cellular induction of endonuclease expression to produce highly localized DSBs have limited temporal resolution (55). The fluorescence three-hybrid assay, used as a control assay in our study, can assess DNA damage-induced interaction between an mEGFP-tagged protein, tethered to the LacO array through a LacI-GFP-nanobody, and an mCherry-tagged protein (25). Due to the abundance of the mEGFP bait tethered at the LacO array, this method offers a highly sensitive detection of protein–protein interaction but lacks quantification of interactions with spatial and temporal resolution.

FRET was chosen for measuring protein–protein interactions at UV laser-induced DNA damage sites as it is quantifiable and allows single-cell analysis of transient or stable interactions between two proteins with high temporal resolution (56). Moreover, FRET only measures direct protein–protein interactions and is thus superior to other methods that are suitable for studying protein–protein interactions in cells but that also detect indirect interactions. FRET has two distinct consequences for the donor fluorophore: reduced fluorescence intensity and reduced fluorescence lifetime. Intensity-based FRET approaches such as acceptor photobleaching require fixation of cells after DNA damage, which can lead to artefacts and precludes the analysis of any transient interactions due to low temporal resolution (41). Unlike intensity-based FRET approaches, FLIM enables robust quantification of FRET based on the reduction in donor lifetime (27). Instead of the traditional FLIM analysis based on curve fittings for calculating donor lifetimes, we employed the phasor approach, which transforms FLIM images into polar plots and provides fluorescence lifetime measurements for laser-induced damage site as well as any other location within the nucleus (30,31).

In addition to FRET, the FLIM microscope is also suitable for fluorescence cross-correlation spectroscopy (FCCS), which is based on correlating the temporal fluctuations of the measured fluorescence intensity of two fluorescently labelled proteins that occur in confocal (∼femtolitre) volume (57). FCCS is particularly suitable for large proteins and was used to measure interaction between DNA repair proteins BRCA2 and RAD51 at DNA breaks randomly induced by ionizing radiation (58). However, precise and spatially defined quantification of protein–protein interactions necessitates localized DNA damage induction combined with 2D imaging, which is now made possible with the UV-FLIM set-up.

FLIM-FRET can be used to study chromatin compaction dynamics by measuring FRET between fluorescently tagged histones at the site of near-infrared (NIR) laser damage (20). FLIM-FRET was also harnessed for studying PARylation dynamics at NIR laser-induced DNA damage sites using a TMR-labelled NAD^+ analogue as a PARP1 cofactor, which is incorporated into PAR (59). Using EGFP-labelled PARP1 or PAR binding protein as a donor in combination with the TMR-labelled PAR as an acceptor allows measurement of PARP1 auto-modification or PAR binding at laser-induced DNA damage sites (59).

The UV-FLIM-FRET system presented in this study enables quantification of protein–protein interactions at UV laser-induced DNA damage sites. We showed that the UV-FLIM-FRET system has the power to temporally and spatially distinguish between three different types of interactions: (i) DNA damage-induced interaction (e.g. PARP1–ALC1, PARP1–XRCC1); (ii) interaction under basal conditions that increases after DNA damage (e.g. ALC1–XRCC1, ALC1–TRIM33); and (iii) comparable interaction under basal and DNA damage conditions (e.g. PARG–PCNA). Using the UV-FLIM-FRET system, we revealed the dynamic interactions between different DDR proteins and found that in all cases DNA damage-induced interaction is dependent on PAR as mutations that impair PARylation or PAR binding abrogate interaction between these protein pairs. This system is, however, not limited to PAR-mediated interactions and can be applied for studying the whole range of DDR proteins. Taken together, UV-FLIM-FRET is the method of choice for studying DNA damage-dependent protein interactions at a single-cell level and at high temporal resolution.

SUPPLEMENTARY DATA

Supplementary Data are available at NAR Online.

REFERENCES

1. Mortusewicz,O., Fouquerel,E., Ame,J.C., Leonhardt,H. and Schreiber,V. (2011) PARG is recruited to DNA damage sites through poly(ADP-ribose)- and PCNA-dependent mechanisms. *Nucleic Acids Res.*, **39**, 5045–5056.

2. Mortusewicz,O. and Leonhardt,H. (2007) XRCC1 and PCNA are loading platforms with distinct kinetic properties and different capacities to respond to multiple DNA lesions. *BMC Mol. Biol.*, **8**, 81.

3. Mortusewicz,O., Leonhardt,H. and Cardoso,M.C. (2008) Spatiotemporal dynamics of regulatory protein recruitment at DNA damage sites. *J. Cell. Biochem.*, **104**, 1562–1569.

4. Gassman,N.R. and Wilson,S.H. (2015) Micro-irradiation tools to visualize base excision repair and single-strand break repair. *DNA Repair (Amst.)*, **31**, 52–63.

5. Lukas,C., Bartek,J. and Lukas,J. (2005) Imaging of protein movement induced by chromosomal breakage: tiny 'local' lesions pose great 'global' challenges. *Chromosoma*, **114**, 146–154.

6. Mortusewicz,O., Ame,J.C., Schreiber,V. and Leonhardt,H. (2007) Feedback-regulated poly(ADP-ribosyl)ation by PARP-1 is required for rapid response to DNA damage in living cells. *Nucleic Acids Res.*, **35**, 7665–7675.

7. Garbrecht,J., Hornegger,H., Herbert,S., Kaufmann,T., Gotzmann,J., Elsayad,K. and Slade,D. (2018) Simultaneous dual-channel imaging to quantify interdependent protein recruitment to laser-induced DNA damage sites. *Nucleus*, **9**, 474–491.

8. Aleksandrov,R., Dotchev,A., Poser,I., Krastev,D., Georgiev,G., Panova,G., Babukov,Y., Danovski,G., Dyankova,T., Hubatsch,L. *et al.* (2018) Protein dynamics in complex DNA lesions. *Mol. Cell*, **69**, 1046–1061.

9. Izhar,L., Adamson,B., Ciccia,A., Lewis,J., Pontano-Vaites,L., Leng,Y., Liang,A.C., Westbrook,T.F., Harper,J.W. and Elledge,S.J. (2015) A systematic analysis of factors localized to damaged chromatin reveals PARP-dependent recruitment of transcription factors. *Cell Rep.*, **11**, 1486–1500.

10. Kochan,J.A., Desclos,E.C.B., Bosch,R., Meister,L., Vriend,L.E.M., van Attikum,H. and Krawczyk,P.M. (2017) Meta-analysis of DNA double-strand break response kinetics. *Nucleic Acids Res.*, **45**, 12625–12637.

11. Mahadevan,J., Bowerman,S. and Luger,K. (2019) Quantitating repair protein accumulation at DNA lesions: past, present, and future. *DNA Repair (Amst.)*, **81**, 102650.

12. Ahel,D., Horejsi,Z., Wiechens,N., Polo,S.E., Garcia-Wilson,E., Ahel,I., Flynn,H., Skehel,M., West,S.C., Jackson,S.P. *et al.* (2009) Poly(ADP-ribose)-dependent regulation of DNA repair by the chromatin remodeling enzyme ALC1. *Science*, **325**, 1240–1243.

13. Gottschalk,A.J., Timinszky,G., Kong,S.E., Jin,J., Cai,Y., Swanson,S.K., Washburn,M.P., Florens,L., Ladurner,A.G., Conaway,J.W. *et al.* (2009) Poly(ADP-ribosyl)ation directs recruitment and activation of an ATP-dependent chromatin remodeler. *Proc. Natl Acad. Sci. U.S.A.*, **106**, 13770–13774.

14. Kulkarni,A., Oza,J., Yao,M., Sohail,H., Ginjala,V., Tomas-Loba,A., Horejsi,Z., Tan,A.R., Boulton,S.J. and Ganesan,S. (2013) Tripartite motif-containing 33 (TRIM33) protein functions in the poly(ADP-ribose) polymerase (PARP)-dependent DNA damage response through interaction with amplified in liver cancer 1 (ALC1) protein. *J. Biol. Chem.*, **288**, 32357–32369.

15. Sellou,H., Lebeaupin,T., Chapuis,C., Smith,R., Hegele,A., Singh,H.R., Kozlowski,M., Bultmann,S., Ladurner,A.G., Timinszky,G. *et al.* (2016) The poly(ADP-ribose)-dependent chromatin remodeler Alc1 induces local chromatin relaxation upon DNA damage. *Mol. Biol. Cell*, **27**, 3791–3799.

16. El-Khamisy,S.F., Masutani,M., Suzuki,H. and Caldecott,K.W. (2003) A requirement for PARP-1 for the assembly or stability of XRCC1 nuclear foci at sites of oxidative DNA damage. *Nucleic Acids Res.*, **31**, 5526–5533.

17. Breslin,C., Hornyak,P., Ridley,A., Rulten,S.L., Hanzlikova,H., Oliver,A.W. and Caldecott,K.W. (2015) The XRCC1 phosphate-binding pocket binds poly (ADP-ribose) and is required for XRCC1 function. *Nucleic Acids Res.*, **43**, 6934–6944.

18. Azarm,K. and Smith,S. (2020) Nuclear PARPs and genome integrity. *Genes Dev.*, **34**, 285–301.

19. Huletsky,A., de Murcia,G., Muller,S., Hengartner,M., Ménard,L., Lamarre,D. and Poirier,G.G. (1989) The effect of poly(ADP-ribosyl)ation on native and H1-depleted chromatin. A role of poly(ADP-ribosyl)ation on core nucleosome structure. *J. Biol. Chem.*, **264**, 8878–8886.

20. Lou,J., Scipioni,L., Wright,B.K., Bartolec,T.K., Zhang,J., Masamsetti,V.P., Gaus,K., Gratton,E., Cesare,A.J. and Hinde,E. (2019) Phasor histone FLIM-FRET microscopy quantifies spatiotemporal rearrangement of chromatin architecture during the DNA damage response. *Proc. Natl Acad. Sci. U.S.A.*, **116**, 7323–7332.

21. Strickfaden,H., McDonald,D., Kruhlak,M.J., Haince,J.-F., Th'ng,J.P.H., Rouleau,M., Ishibashi,T., Corry,G.N., Ausio,J., Underhill,D.A. *et al.* (2016) Poly(ADP-ribosyl)ation-dependent transient chromatin decondensation and histone displacement following laser microirradiation. *J. Biol. Chem.*, **291**, 1789–1802.

22. Lehmann,L.C., Hewitt,G., Aibara,S., Leitner,A., Marklund,E., Maslen,S.L., Maturi,V., Chen,Y., van der Spoel,D., Skehel,J.M. *et al.* (2017) Mechanistic insights into autoinhibition of the oncogenic chromatin remodeler ALC1. *Mol. Cell*, **68**, 847–859.

23. Singh,H.R., Nardozza,A.P., Möller,I.R., Knobloch,G., Kistemaker,H.A.V., Hassler,M., Harrer,N., Blessing,C., Eustermann,S., Kotthoff,C. *et al.* (2017) A poly-ADP-ribose trigger releases the auto-inhibition of a chromatin remodeling oncogene. *Mol. Cell*, **68**, 860–871.

24. Smith,R., Lebeaupin,T., Juhász,S., Chapuis,C., D'Augustin,O., Dutertre,S., Burkovics,P., Biertümpfel,C., Timinszky,G. and Huet,S. (2019) Poly(ADP-ribose)-dependent chromatin unfolding facilitates the association of DNA-binding proteins with DNA at sites of damage. *Nucleic Acids Res.*, **47**, 11250–11267.

25. Smith,R., Sellou,H., Chapuis,C., Huet,S. and Timinszky,G. (2018) CHD3 and CHD4 recruitment and chromatin remodeling activity at DNA breaks is promoted by early poly(ADP-ribose)-dependent chromatin relaxation. *Nucleic Acids Res.*, **46**, 6087–6098.

26. Day,R.N. and Davidson,M.W. (2012) Fluorescent proteins for FRET microscopy: monitoring protein interactions in living cells. *Bioessays*, **34**, 341–350.

27. Becker,W. (2012) Fluorescence lifetime imaging: techniques and applications. *J. Microsc.*, **247**, 119–136.

28. Kaufmann,T., Grishkovskaya,I., Polyansky,A.A., Kostrhon,S., Kukolj,E., Olek,K.M., Herbert,S., Beltzung,E., Mechtler,K., Peterbauer,T. *et al.* (2017) A novel non-canonical PIP-box mediates PARG interaction with PCNA. *Nucleic Acids Res.*, **45**, 9741–9759.

29. Ronson,G.E., Piberger,A.L., Higgs,M.R., Olsen,A.L., Stewart,G.S., McHugh,P.J., Petermann,E. and Lakin,N.D. (2018) PARP1 and PARP2 stabilise replication forks at base excision repair intermediates through Fbh1-dependent Rad51 regulation. *Nat. Commun.*, **9**, 746.

30. Digman,M.A., Caiolfa,V.R., Zamai,M. and Gratton,E. (2008) The phasor approach to fluorescence lifetime imaging analysis. *Biophys. J.*, **94**, L14–L16.

31. Hinde,E., Digman,M.A., Welch,C., Hahn,K.M. and Gratton,E. (2012) Biosensor Förster resonance energy transfer detection by the phasor approach to fluorescence lifetime imaging microscopy. *Microsc. Res. Tech.*, **75**, 271–281.

32. Niehörster,T., Löschberger,A., Gregor,I., Krämer,B., Rahn,H.-J., Patting,M., Koberling,F., Enderlein,J. and Sauer,M. (2016) Multi-target spectrally resolved fluorescence lifetime imaging microscopy. *Nat. Methods*, **13**, 257–262.

33. Abdollahi,E., Taucher-Scholz,G. and Jakob,B. (2018) Application of fluorescence lifetime imaging microscopy of DNA binding dyes to assess radiation-induced chromatin compaction changes. *Int. J. Mol. Sci.*, **19**, 2399.

34. Tramier,M., Zahid,M., Mevel,J.C., Masse,M.J. and Coppey-Moisan,M. (2006) Sensitivity of CFP/YFP and GFP/mCherry pairs to donor photobleaching on FRET determination by fluorescence lifetime imaging microscopy in living cells. *Microsc. Res. Tech.*, **69**, 933–939.

35. Dale,R.E., Eisinger,J. and Blumberg,W.E. (1979) The orientational freedom of molecular probes. The orientation factor in intramolecular energy transfer. *Biophys. J.*, **26**, 161–193.

36. Broussard,J.A., Rappaz,B., Webb,D.J. and Brown,C.M. (2013) Fluorescence resonance energy transfer microscopy as demonstrated by measuring the activation of the serine/threonine kinase Akt. *Nat. Protoc.*, **8**, 265–281.

37. Kong,X., Mohanty,S.K., Stephens,J., Heale,J.T., Gomez-Godinez,V., Shi,L.Z., Kim,J.S., Yokomori,K. and Berns,M.W. (2009) Comparative analysis of different laser systems to study cellular responses to DNA damage in mammalian cells. *Nucleic Acids Res.*, **37**, e68.

38. Tashiro,S., Walter,J., Shinohara,A., Kamada,N. and Cremer,T. (2000) Rad51 accumulation at sites of DNA damage and in postreplicative chromatin. *J. Cell Biol.*, **150**, 283–292.

39. Lan,L., Nakajima,S., Oohata,Y., Takao,M., Okano,S., Masutani,M., Wilson,S.H. and Yasui,A. (2004) *In situ* analysis of repair processes for oxidative DNA damage in mammalian cells. *Proc. Natl Acad. Sci. U.S.A.*, **101**, 13738–13743.

40. Turgeman,L. and Fixler,D. (2014) The influence of dead time related distortions on live cell fluorescence lifetime imaging (FLIM) experiments. *J. Biophotonics*, **7**, 442–452.

41. Zeug,A., Woehler,A., Neher,E. and Ponimaskin,E.G. (2012) Quantitative intensity-based FRET approaches: a comparative snapshot. *Biophys. J.*, **103**, 1821–1827.

42. Herce,H.D., Deng,W., Helma,J., Leonhardt,H. and Cardoso,M.C. (2013) Visualization and targeted disruption of protein interactions in living cells. *Nat. Commun.*, **4**, 2660.

43. Hanzlikova,H., Gittens,W., Krejcikova,K., Zeng,Z. and Caldecott,K.W. (2017) Overlapping roles for PARP1 and PARP2 in the recruitment of endogenous XRCC1 and PNKP into oxidized chromatin. *Nucleic Acids Res.*, **45**, 2546–2557.

44. Polo,L.M., Xu,Y., Hornyak,P., Garces,F., Zeng,Z., Hailstone,R., Matthews,S.J., Caldecott,K.W., Oliver,A.W. and Pearl,L.H. (2019) Efficient single-strand break repair requires binding to both poly(ADP-ribose) and DNA by the central BRCT domain of XRCC1. *Cell Rep.*, **26**, 573–581.

45. Mortusewicz,O., Amé,J.-C., Schreiber,V. and Leonhardt,H. (2007) Feedback-regulated poly(ADP-ribosyl)ation by PARP-1 is required for rapid response to DNA damage in living cells. *Nucleic Acids Res.*, **35**, 7665–7675.

46. Agricola,E., Randall,R.A., Gaarenstroom,T., Dupont,S. and Hill,C.S. (2011) Recruitment of TIF1γ to chromatin via its PHD finger-bromodomain activates its ubiquitin ligase and transcriptional repressor activities. *Mol. Cell*, **43**, 85–96.

47. Barkauskaite,E., Jankevicius,G. and Ahel,I. (2015) Structures and mechanisms of enzymes employed in the synthesis and degradation of PARP-dependent protein ADP-ribosylation. *Mol. Cell*, **58**, 935–946.

48. Polo,S.E., Kaidi,A., Baskcomb,L., Galanty,Y. and Jackson,S.P. (2010) Regulation of DNA-damage responses and cell-cycle progression by the chromatin remodelling factor CHD4. *EMBO J.*, **29**, 3130–3139.

49. Chou,D.M., Adamson,B., Dephoure,N.E., Tan,X., Nottke,A.C., Hurov,K.E., Gygi,S.P., Colaiácovo,M.P. and Elledge,S.J. (2010) A chromatin localization screen reveals poly(ADP ribose)-regulated recruitment of the repressive polycomb and NuRD complexes to sites of DNA damage. *Proc. Natl Acad. Sci. U.S.A.*, **107**, 18475–18480.

50. Smits,A.H. and Vermeulen,M. (2016) Characterizing protein–protein interactions using mass spectrometry: challenges and opportunities. *Trends Biotechnol.*, **34**, 825–834.

51. Mishra,P.K., Yoo,C.M., Hong,E. and Rhee,H.W. (2019) Photo-crosslinking: an emerging chemical tool for investigating molecular networks in live cells. *ChemBioChem*, **21**, 924–932.

52. Samavarchi-Tehrani,P., Samson,R. and Gingras,A.C. (2020) Proximity dependent biotinylation: key enzymes and adaptation to proteomics approaches. *Mol. Cell. Proteomics*, **19**, 757–773.

53. Cui,Y., Zhang,X., Yu,M., Zhu,Y., Xing,J. and Lin,J. (2019) Techniques for detecting protein–protein interactions in living cells: principles, limitations, and recent progress. *Sci. China Life Sci.*, **62**, 619–632.

54. Weibrecht,I., Leuchowius,K.J., Clausson,C.M., Conze,T., Jarvius,M., Howell,W.M., Kamali-Moghaddam,M. and Soderberg,O. (2010) Proximity ligation assays: a recent addition to the proteomics toolbox. *Expert Rev. Proteomics*, **7**, 401–409.

55. Polo,S.E. and Jackson,S.P. (2011) Dynamics of DNA damage response proteins at DNA breaks: a focus on protein modifications. *Genes Dev.*, **25**, 409–433.

56. Okamoto,K. and Sako,Y. (2017) Recent advances in FRET for the study of protein interactions and dynamics. *Curr. Opin. Struct. Biol.*, **46**, 16–23.

57. Lakowicz,J.R. (2006) In: *Principles of Fluorescence Microscopy*, 3rd edn. Springer, Berlin.

58. Jeyasekharan,A.D., Ayoub,N., Mahen,R., Ries,J., Esposito,A., Rajendra,E., Hattori,H., Kulkarni,R.P. and Venkitaraman,A.R. (2010) DNA damage regulates the mobility of Brca2 within the nucleoplasm of living cells. *Proc. Natl Acad. Sci. U.S.A.*, **107**, 21937–21942.

59. Buntz,A., Wallrodt,S., Gwosch,E., Schmalz,M., Beneke,S., Ferrando-May,E., Marx,A. and Zumbusch,A. (2016) Real-time cellular imaging of protein poly(ADP-ribos)ylation. *Angew. Chem. Int. Ed. Engl.*, **55**, 11256–11260.